Missouri University of Science and Technology
Scholars' Mine

Mechanical and Aerospace Engineering Faculty Research & Creative Works

Mechanical and Aerospace Engineering

01 Jul 2022

In-Situ Infrared Thermographic Inspection for Local Powder Layer Thickness Measurement in Laser Powder Bed Fusion

Tao Liu

Cody S. Lough

Hossein Sehhat

Yi Ming Ren

et. al. For a complete list of authors, see https://scholarsmine.mst.edu/mec_aereng_facwork/4936

Follow this and additional works at: https://scholarsmine.mst.edu/mec_aereng_facwork

 Part of the Aerospace Engineering Commons, and the Mechanical Engineering Commons

Recommended Citation

T. Liu et al., "In-Situ Infrared Thermographic Inspection for Local Powder Layer Thickness Measurement in Laser Powder Bed Fusion," *Additive Manufacturing*, vol. 55, article no. 102873, Elsevier, Jul 2022.
The definitive version is available at https://doi.org/10.1016/j.addma.2022.102873

This Article - Journal is brought to you for free and open access by Scholars' Mine. It has been accepted for inclusion in Mechanical and Aerospace Engineering Faculty Research & Creative Works by an authorized administrator of Scholars' Mine. This work is protected by U. S. Copyright Law. Unauthorized use including reproduction for redistribution requires the permission of the copyright holder. For more information, please contact scholarsmine@mst.edu.

Additive Manufacturing 55 (2022) 102873

Contents lists available at ScienceDirect

Additive Manufacturing

journal homepage: www.elsevier.com/locate/addma

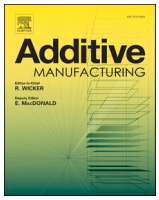

Research paper

In-situ infrared thermographic inspection for local powder layer thickness measurement in laser powder bed fusion

Tao Liu [a,*], Cody S. Lough [a], Hossein Sehhat [a], Yi Ming Ren [b], Panagiotis D. Christofides [b], Edward C. Kinzel [c], Ming C. Leu [a]

[a] Mechanical and Aerospace Engineering Department, Missouri University of Science and Technology, Rolla, MO 65409, USA
[b] Chemical and Biomolecular Engineering Department, University of California, Los Angeles, CA 90095, USA
[c] Aerospace and Mechanical Engineering Department, University of Notre Dame, Notre Dame, IN 46556, USA

ARTICLE INFO

Keywords:
Laser powder bed fusion (LPBF)
Infrared thermography
Powder thickness
Recoater crash
Neural network
Additive manufacturing

ABSTRACT

The laser powder bed fusion (LPBF) process is strongly influenced by the characteristics of the powder layer, including its thickness and thermal transport properties. This paper investigates in-situ characterization of the powder layer using thermographic inspection. A thermal camera monitors the temperature history of the powder surface immediately after a layer of new powder is deposited by the recoating system. During this process, thermal energy diffuses from the underlying solid part, eventually raising the temperature of the above powder layer. Guided by 1D modeling of this heat-up process, experiments show how the parameterized thermal history can be correlated with powder layer thickness and its thermal conductivity. A neural network, based on the parameterized thermal history, further improves the correlation after training. It is used to predict the part distortion for an unsupported structure. This method detects serious part distortion several layers before the part breaks through the powder layer and interacts with the recoater. This approach can be automated to prevent catastrophic recoater crashes or abrasion of soft wipers and has the potential to monitor local properties of the powder layer in-situ.

1. Introduction

The process dynamics of laser powder bed fusion (LPBF) have received considerable study. In particular, both experimental and computational studies have shown how the process parameters, e.g. laser power and scan speed, affect the local properties of the part, e.g. porosity. In-situ diagnostics have also focused on monitoring the melt pool and several research groups have shown significant correlations between radiative signatures and the local part quality. While it has not received as much attention, the properties of the powder layer, particularly the thickness, also has a significant influence on the local melt pool and overall properties of the part. In general, a thicker powder layer increases the production rate but can lead to porosity due to lack of fusion [1]. Also, if the powder layer becomes too thin, it becomes discontinuous with vacancies that can negatively affect the final part porosity [2–4]. The powder layer thickness has been shown to affect the melt pool size [5], grain size [6], density [7], microhardness [6,7], surface roughness [8], strength, and elasticity [9,10] of the produced part.

The nominal powder layer thickness can be specified for each layer by controlling the elevator step size in between layers. However, unlike other process parameters (e.g. laser power, scan-speed, beam path), there is less control authority for powder layer thickness, both overall and locally. At a global level, consolidation of the powder on the first few layers, leads to a substantial increase in powder thickness over the nominal build layer thickness [11,12]. Locally, the powder thickness is affected by thermal distortion of the part as the separation between the part and the wiper changes. The thinner powder bed layers also have been shown to increase the thermally induced residual stresses [13–15]. This is particularly a concern for overhanging structures, where the unsupported edge bends away from the build plate and reduces the powder layer thickness. The reduction in powder layer thickness feedbacks to higher local temperatures, producing more part distortion and resulting in further reductions in powder layer thickness in subsequent layers. This cycle can progress rapidly and lead to interference between the part and the recoater, equivalent to a negative powder layer

* Corresponding author.
E-mail address: tlkv5@umsystem.edu (T. Liu).

https://doi.org/10.1016/j.addma.2022.102873
Received 15 February 2022; Received in revised form 30 April 2022; Accepted 2 May 2022
Available online 6 May 2022
2214-8604/© 2022 The Author(s). Published by Elsevier B.V. This is an open access article under the CC BY-NC-ND license (http://creativecommons.org/licenses/by-nc-nd/4.0/).

thickness. In the case of soft wipers, this interaction leads to abrasion of the wiper surface which can affect all the parts in line with the damage region (increasing the local powder layer thickness). For a rigid wiper, the interference leads to a collision, which stops the motion of the recoater or damages it. Recoater crashes are a widespread failure and impedes the automation of additive manufacturing processes such as LPBF [16].

Monitoring the surface with high-resolution optical imaging can capture regions of the build not fully covered by powder after the recoating step [17,18]. While this can capture a part that has broken through the powder layer, it does not resolve local variances in powder thickness, which would provide advanced warning of part distortion, and could potentially be used in feedback control. Several techniques have been developed to measure the part height after laser consolidation and this can be used to infer the powder layer thickness. For example, Williams et al. [19] used a fixed laser displacement to measure the local height of the powder layer and consolidated material. DePond et al. [20] presented a technique using optical coherence tomography (OCT) to generate a high-resolution point-by-point map of the part height. Several groups have studied fringe projection techniques to measure part height [21–23]. These techniques require pausing the process to measure the height which adds time to the print.

This paper investigates a thermography based technique to estimate the powder bed thickness. Infrared thermography uses the diffusion of heat through a material to evaluate the material properties [24] including the thermal diffusivity and optical absorption coefficient [25], as well as discontinuities such as sub-surface cracks or defects and coating thicknesses [26]. The surface temperature is observed using a thermal camera and the heat source forcing the thermal diffusion can be active or passive [27,28]. The information about the thermal transport is often dynamic and a wide range of techniques to evaluate process transient thermal histories have been developed, particularly for active thermography where there is temporal control of the heat source [29–32].

In this paper, the printed part serves as the heat source, which retains heat from the deposition process. This heating can be supplemented by a heated build plate but is not required. When the recoating process spreads relatively cool powder over the previously deposited region, heat diffuses through powder to its top surface. The temperature history of the top surface is observed with a thermal camera. The transient thermal response is a function of the layer thickness as well as the thermal properties of the powder layer. For a powder with constant thermal properties, the transient response can be parameterized and these signatures correlated with layer thickness.

Thermal cameras are present in many LPBF machines, particularly research installations, and are used to monitor thermal features during additive manufacturing [33]. Short-wavelength infrared (SWIR) and long-wavelength infrared (LWIR) cameras combined with visible camera have been used to measure melt-pool dimensions [34], cooling rate [35], thermal distortion [36], surface temperature [37,38], and thermal history [39]. This is largely motivated by defect detection. A number of data-driven approaches aid in relating signatures to thermal features to defects or properties [40]. In particular, machine learning algorithms have been used to process imaging data to efficiently assess the part quality and detect build defects [41,42]. This data-based method to train a detection algorithm for potential errors is widely used due to its robust performance for an extensive range of operating conditions. Among advanced machine-learning methods, feed-forward neural networks (FNN) have successfully performed regression tasks in many applications [43,44]. This paper shows how a FFN improves on a simple physics based regression by allowing more feature data to be included in the correlation.

The paper is organized as follows. The experimental setup, including the configuration of the thermal camera, and representative thermal histories are first presented. A 1D thermal model is developed and used to suggest a parameterization for the thermal history. The rise time is extracted from this parameterization. The measured rise time is correlated with experimental powder bed thicknesses for a calibration specimen. This data is compared to the 1D model to provide an estimate for the thermal conductivity. Next, all the parameterized data is used with FNN to improve the ability to predict powder layer thickness. This is validated by monitoring the powder layer thickness for a printed part with an overhang. This experiment also shows the potential to predict the interaction with the wiper 10 layers before it occurs. The thermographic inspection technique is shown to have significant potential for monitoring the powder bed thickness and can be expanded to detect variations in the powder properties. This has the potential to limit recoater/part collisions which are a common failure in LPBF. Monitoring the powder layer health is critical to ensuring part quality. The technique requires a relatively low cost thermal camera, but by using the powder spreading process, the inspection technique does not add delays or otherwise modify the LPBF process. These advantages may make the approach attractive for industrial adoption.

2. Experimental setup

Fig. 1 illustrates the experimental setup with a long-wavelength infrared (LWIR) camera (FLIR A655sc) integrated with a commercial LPBF machine (Renishaw AM250). A ZnSe window on the chamber allows the LWIR camera to observe the build plate from 15° off-normal. The LWIR camera has 640 × 480 pixels which corresponds to a spatial resolution of 325 μm in this configuration. The spectral range of this LWIR camera is 7.5–14.0 μm. The noise-equivalent temperature difference (NETD) is 30 mK and frame rate is 200 Hz. The camera reports the temperature of the scene assuming an emissivity of 0.95 (gray body approximation) and is not corrected for transmission through the window. Because the emissivity of the powder and the printed solid material as well as the wiper differ, the measured temperatures are lower than the true temperatures. However, the relevant information for the procedure presented in this paper is in the time domain. This allows the measured temperatures to be normalized for calculations and removes requirements for emissivity and non-uniformity calibrations, significantly simplifying the instrumentation.

Fig. 2 shows the temperature history of a single pixel for a 67.6 s duration layer during a typical build using 304 L stainless steel powder in a Renishaw AM250. The powder used in this paper had diameters ranging between 15 and 40 μm with a mean diameter 25 μm. At the start of the process, powder is dispensed from the hopper at the back of the chamber. The wiper spreads the powder over the build area, traveling from the back of the chamber to the front of the chamber. The time index is shifted so that the wiper passes over the pixel in Fig. 2 at $t = 0$. As the wiper completes its travel, it pushes any excess powder into a catchment

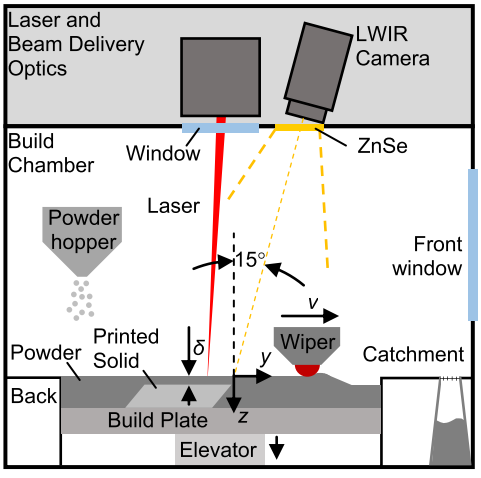

Fig. 1. Illustration of the LPBF experimental setup including the LWIR camera.

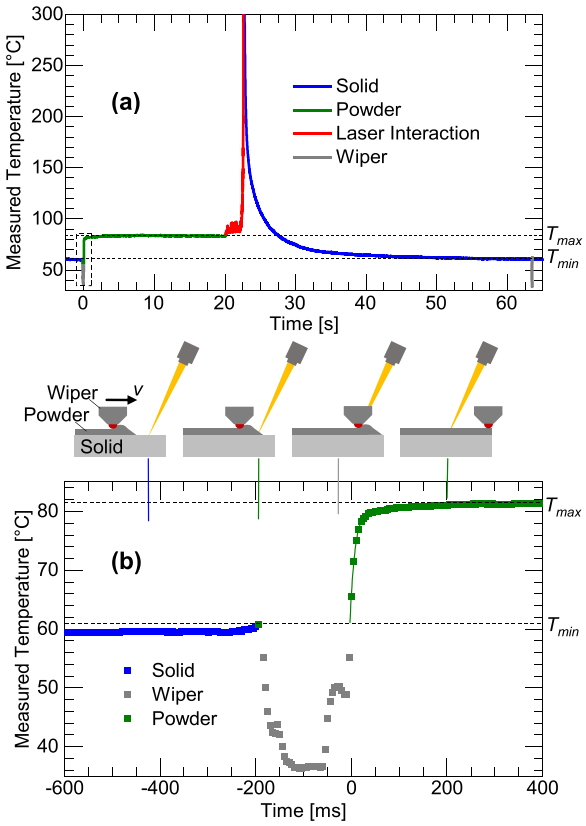

Fig. 2. Temperature history of a single pixel, for (a) one complete layer and (b) new powder layer heating process with insets highlighting the changes of emissivity of the pixel.

at the front of the chamber. The laser is then scanned over the pattern for the layer to fuse the powder to the part. The camera captures this interaction but is saturated when the pixel is heated directly by the laser. At the conclusion of the laser patterning, the build plate is lowered by the layer height, δ, and the wiper returns to the back of the chamber, passing back over the pixel at $t = 63.5$ s. The emissivity of the pixel changes depending on the states of the material and presence of the wiper. These changes are indicated by the color of the trace.

Fig. 2(b) shows a close-up of the interaction with the wiper during the powder-spreading step. Initially the pixel corresponds to the printed part which has a lower emissivity. This has cooled from the interaction with the laser, although there still retains some residual heat as well as any heating from the build plate (maintained at 80 °C for the builds). The wiper pushes powder in front of it. Some of this powder enters the pixel before the wiper. Although the fresh powder is cooler, the increased emissivity leads to a slight increase in the measured temperature to T_{min} at $T = 60.75$ °C. When the wiper blocks the camera's view of the pixel there is a decrease in the measured temperature (indicated in grey), followed by a sharp rise in the measured temperature ($t = 0$). The surface temperature of the powder increases as heat diffuses from the underlying part. This asymptotically approaches a steady state value of T_{max}, which is the temperature of the build plate i.e. $T_{max} = T_s = 80$ °C. It should be noted that both T_{min} and T_{max} have the same emissivity because they both correspond to the powder state.

The dynamic response of the surface temperature is a function of the powder layer thickness as well as the thermal properties of the powder. The remainder of the paper focuses on this portion of the temperature-time history. It is convenient to normalize the local surface temperature by

$$T' = \frac{T - T_{\min}}{T_{\max} - T_{\min}} \tag{1}$$

which removes the effects of the temperature of the underlying part as well as the dependence on the camera's calibration.

3. 1D heat transfer model and finite difference solution

3.1. 1D heat transfer model

Insight into the temperature history can be achieved from modeling the thermal diffusion through the powder from the underlying part. While the powder layer is made of discrete particles, evaluating it as continuous effective medium significantly simplifies the analysis. Also, the thickness of the powder is much less than the lateral extent of most parts, so it is reasonable to model the problem as 1D problem in the z-direction. Lastly, the temperature range for the system during the recoating step does not vary significantly enough to consider thermally dependent properties. Fig. 3(a) illustrates this model. A powder layer of thickness, δ, is in contact with the printed solid part. Radiation exchange at the free surface of the powder is neglected, but a convection boundary condition is applied. The printed solid part is modeled as semi-infinite. The temperature of the semi-infinite end side is constant temperature at $T_s = 80$ °C. This problem is governed by the heat transfer equation,

$$\frac{\partial T}{\partial t} = \frac{k_i}{\rho_i c_i}\frac{\partial^2 T}{\partial z^2} \tag{2}$$

with boundary conditions,

$$k_p \left.\frac{\partial T}{\partial z}\right|_{z=0} = h[T(z=0,t) - T_\infty] \tag{3}$$

$$T(z \to \infty, t) = T_s \tag{4}$$

and initial condition

$$T(z, t=0) = \begin{cases} T_p & 0 < z < \delta \\ T_s & \delta < z \end{cases} \tag{5}$$

where T is the temperature and is a function of time, t, and distance from the surface of the powder, z. The thermal properties in Eq. (2) depend on the material and can be either powder or printed solid (denoted by the subscript, i, which is p for powder and s for printed solid). k, ρ and c are the effective thermal conductivity, density and specific heat of the materials. h is the convection heat transfer coefficient. T_∞ is the ambient temperature while T_s and T_p are the initial temperatures of the printed solid and powder, respectively.

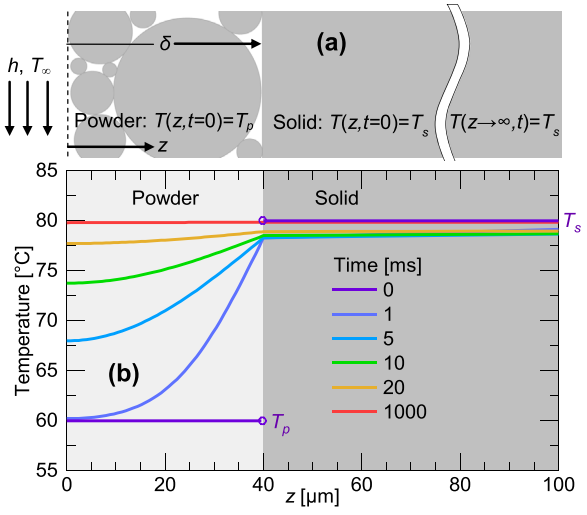

Fig. 3. 1D heat diffusion model (a) model definition and (b) simulated temperature distribution at various times.

The temperature distribution is solved using a finite difference method using material properties shown in Table 1 [45,46]. The powder's effective thermal conductivity is fit from experiments as described in Section 4.2. The calculated temperature distribution is shown as a function of depth z in Fig. 3(b) for T_s= 80 °C, T_p= 60 °C, T_∞= 60 °C, h= 15 W/m^{2}K. The thermal camera only has access to the surface temperature of the powder. The model predicts that the powder surface temperature approaches the steady state within almost 1 s.

3.2. Thermal feature: rise time

It is helpful to have a parameterized expression to fit to the surface temperature history. The following equation captures the surface temperature rise predicted by the finite difference solution to Eqs. (2)–(5).

$$T(z=0,t) = A_1 - A_2 e^{-\beta_1 (t-t_i)} - A_3 e^{-\beta_2 (t-t_i)} \qquad t > t_i \tag{6}$$

where A_1 is the powder free surface's steady-state temperature and A_1-A_2-A_3 is the powder free surface's initial temperature, T_p. Replacing t with t-t_i allows the time history to be shifted so the initial condition occurs at t_i (when the wiper introduces fresh powder to the printed solid surface). The coefficients β_1 and β_2 depend on the powder layer thickness and thermal diffusivity of the materials. For a sufficiently thick powder layer on a high thermal diffusivity material ($\alpha = k/\rho c$), it can be shown that $\beta \propto \alpha_p/\delta^2$. While this serves as a starting point, it breaks down for thinner powder layers and this paper fits the coefficients numerically for both simulation and experiments. After normalization using Eq. (1), the initial temperature of powder free surface $T'(z=0,t=t_i)$ is zero, so that A_1-A_2-$A_3 = 0$ and Eq. (6) can be simplified as

$$T'(z=0,t) = A_1 - A_2 e^{-\beta_1 (t-t_i)} - (A_1 - A_2) e^{-\beta_2 (t-t_i)} \qquad t > t_i. \tag{7}$$

The coefficients A_1, A_2, β_1, β_2 and t_i can be fit to the free surface temperature. Fig. 4(a) shows the ability of Eq. (7) to capture the free surface temperature predicted by the finite difference model for different powder layer thicknesses. The mean squared error for the powder thicknesses in Fig. 4(a) is less than 5.3×10^{-6}.

A characteristic rise time, τ, defined as the time from t-t_i for the surface temperature to reach 90% of steady state, can be obtained from Eq. (7).

$$A_2 e^{-\beta_1 \tau} + (A_1 - A_2) e^{-\beta_2 \tau} = 0.1 A_1 \tag{8}$$

The rise time serves as a thermal feature which can be related to the powder layer thickness or the thermal properties. Fig. 4(b) shows the dependence of the rise time on the powder layer thickness from finite difference model calculated results. This relationship is captured by a power law dependence

$$\delta = 296.8 \tau^{0.5048}. \tag{9}$$

Assuming the constant properties in Table 1, this function can be used to predict the powder thickness δ from rise-time τ, which can be fit to simulated or experimental data. The uncertainty in the predicted powder layer thickness depends on the first derivative of Eq. (9). An estimate for the uncertainty in the powder layer thickness, $\Delta\delta$ is given by

$$\Delta\delta = \frac{\partial \delta}{\partial \tau} \Delta\tau \tag{10}$$

where $\Delta\tau$ is the uncertainty in the rise time. For example, if we assume that the uncertainty in the time constant scales with the reciprocal of the frame rate of the camera (200 Hz), the uncertainty for a 40 μm powder layer would be 5.21 μm while the uncertainty for a 100 μm decreases to 2.17 μm. Coincidentally, this agrees with the breakdown in the treatment of the powder layer as an effective medium as the layer thickness approaches the powder particle diameter (40 μm for the powder in this paper).

Table 1
Material properties of 304 L solid and powder.

Properties	304 L Solid	304 L Powder
Density, ρ [kg/m^3]	8030	4818
Specific heat capacity, c [J/kg·K]	490	490
Thermal conductivity, k [W/m·K]	16.2	0.269

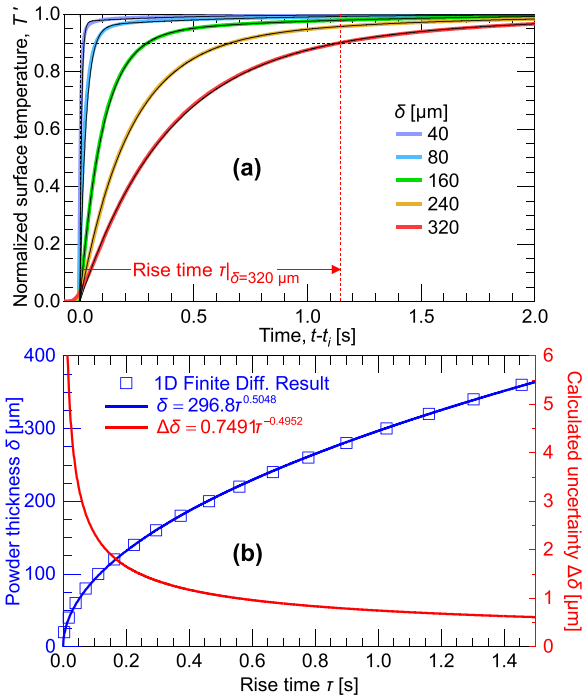

Fig. 4. Fitted 1D thermal diffusion model results (a) parameterized fitted results overlayed on results from finite difference solution with rise time for the δ = 320 μm layer highlighted (b) powder thickness as a function of rise time with power law fit and calculated powder layer thickness uncertainty.

4. Experimental validation

4.1. Calibration to experimental powder thickness

The parametric expressions in Eqs. (7) and (8) can also be applied to experimentally gathered data, and the experimentally fit coefficients can then be used to predict the powder thickness. This approach requires collection of temperature histories for various known powder thicknesses. Fig. 5(a) and (b) shows a simple gage specimen printed with the Renishaw AM250. It consists of 5 mm wide strips, 35 mm long, at different elevations h from a printed datum plane. After the specimen was printed, the unfused powder is removed from above the gage specimen. The specimen is not removed from the build platform. After the powder is removed the chamber is resealed again, the argon atmosphere restored, and the build plate heated to 80 °C, before commanding the system to add a new layer of powder. The wiper then spreads powder over the build plate including the specimen. This gives a powder layer thickness that varies spatially with the height of the individual strips of the gage specimen. The powder layer thickness is $\delta = h_0$-h, where h_0 is the height above the datum of the build plane. In this experiment h_0 = 360 μm so that the highest specimen has δ = 40 μm of powder above it. The heights of the gage specimen and corresponding powder thicknesses are listed in Table 2. The 8 different heights in the table are repeated three times along the width of the specimen. The thermal histories for each pixel above the specimen are recorded during the recoating process. After this, the build plate is removed from chamber and cleaned. The top surface of the specimen is then laser scanned (LMI Gocater 2320) to measure precisely and map the height of each strip

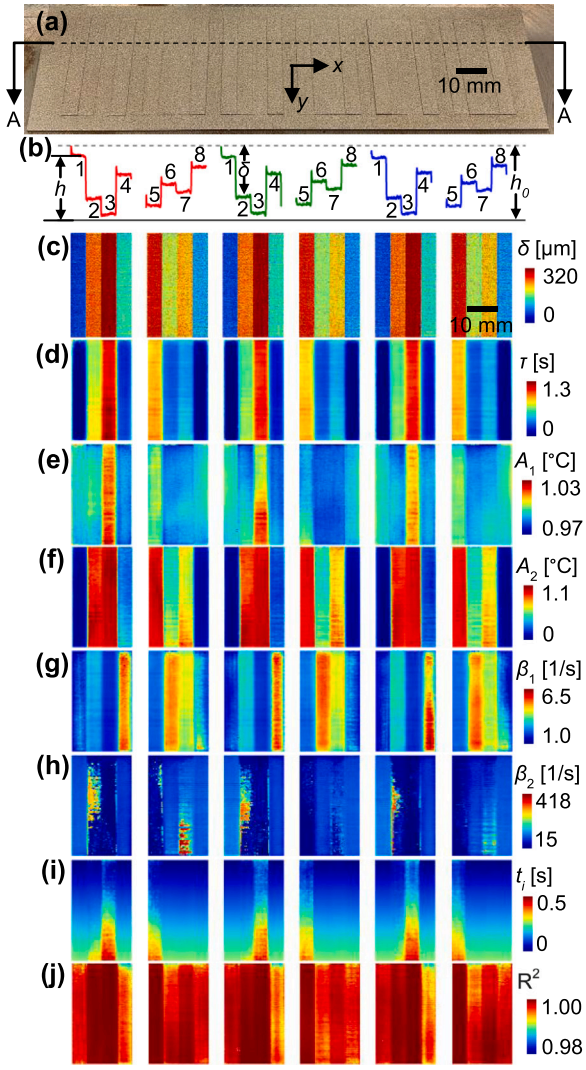

Fig. 5. (a) Photograph of height artifact and (b) surface profile along cross section A-A. 2D maps of the (c) measured powder layer thickness, (d) rise-time τ, (e) A_1, (f) A_2, (g) β_1, (h) β_2, (i) t_i, (j) coefficient of determination ^{2}.

Table 2
The height of each of the eight different strips and corresponding powder thickness δ.

n	h [μm]	δ [μm]
1	320	40
2	120	240
3	40	320
4	240	120
5	80	280
6	200	160
7	160	200
8	280	80

above the datum plane. Fig. 5(b) shows the measured height of each specimen and Fig. 5(c) shows a spatial map of the corresponding powder thickness registered to the camera pixels. This shows minimal local variances from the nominal powder thickness.

Fig. 6(a) shows examples of the temperature histories for pixels with different nominal powder thicknesses. Eq. (7) is fit to the temperature history pixel-by-pixel. The five fitted coefficients are plotted in Fig. 5(e)-(i). As mentioned in Section 3.2, A_1 corresponds to the normalized steady state temperature and should have a nominal value of unity.

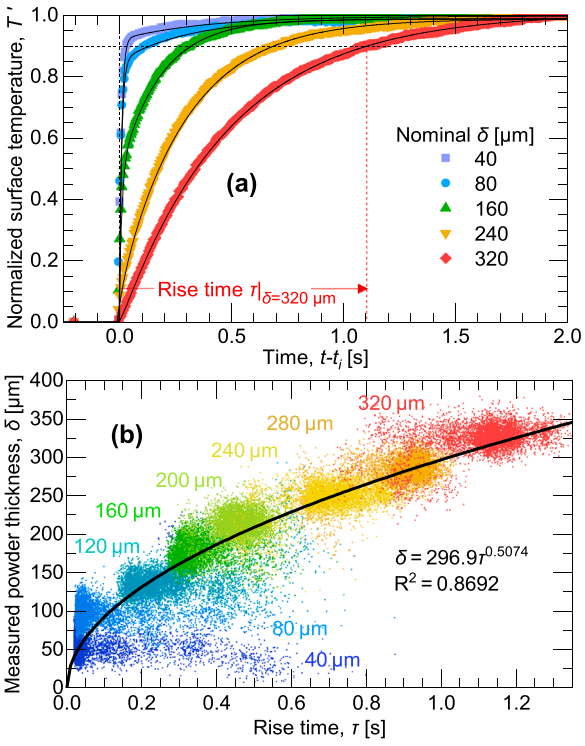

Fig. 6. (a) Measured temperature histories for different powder thicknesses and fitted parameters (b) powder thickness δ with respect to rise-time τ.

Fig. 5(e) shows that the fitted values of A_1 range between 0.97 and 1.03. The time shift t_i is related to when the wiper passes over the pixel. The coefficient β_1 is inversely proportionate to the thickness of the powder layer as should be expected. Fig. 5(f) shows that t_i scales linearly with y for thinner powder layers. This agrees with the constant velocity (v=140 mm/s) of the wiper in the y-direction. For thicker powder layers, there is a delay between when the powder is deposited and when a temperature rise can be observed on the free surface because of the time it takes for thermal energy to diffuse through the powder layer.

The coefficient of determination, R^2, for these fits is shown in Fig. 5 (j). The figure shows that Eq. (7) captures the local temperature histories well and the minimum R^2 over the entire gage specimen is 0.98 with an average for all the data of $R^2 = 0.997$. The five fitted coefficients can be combined using Eq. (8) to calculate the rise time for each pixel. This is plotted in Fig. 5(d). The correspondence between powder layer thickness and rise time is clearly visible in Fig. 5(c) and (d). Fig. 6(b) also shows the powder layer thickness as a function of rise time. A power law fit to this data gives the relationship

$$\delta = 296.9\tau^{0.5074}. \tag{11}$$

which has $R^2 = 0.869$.

While the parameterization from the 1D model captures the response well for the interior of the strips as illustrated in Fig. 6(a), Fig. 6(b) shows significant scatter in the rise time and the measured powder thickness. Much of this occurs at the boundary between strips. In these regions, the assumptions of the 1D model are not satisfied and the thermal disturbance spreads laterally (cylindrically away from the edge defined by the adjacent strips). Experimentally, this lateral spread is on the order of two pixels (0.65 mm for this setup) and is convoluted with resolution of the camera.

4.2. Powder thermal conductivity

The temperature history also depends on the thermal properties of the powder layer. Fig. 7(a) shows the predicted relationship between the

rise time and powder layer thickness for different effective thermal conductivities of the powder, k_p, calculated using the 1D heat transfer model in Section 3. As expected, the rise time scales inversely to the thermal conductivity. Fig. 7(a) also shows the experimental data from Fig. 6(b) again and suggests that the effective thermal conductivity can be fit to the experimental data. Fig. 7(b) shows the coefficient of determination R^2 for fitting experimental data with the 1D diffusion model results obtained using different effective thermal conductivities. A third order polynomial is used to fit the data and has the maximum when the powder's effective thermal conductivity k_p is 0.269 W/m·K. This agrees with the experimentally measured thermal conductivity for 316 L stainless steel powder in Lien et al. [46]. While the same approach could be used to estimate the powder's other thermal properties, the density and specific heat are more straightforward to measure experimentally. This analysis suggests that local changes in the powder properties, including density, can be detected using a thermal camera to monitor the thermal diffusion through the powder.

5. Basic machine learning with FNN regression learner for powder thickness prediction

The previous section showed that working with the rise time leads to straightforward correlations to the powder thickness or thermal properties. However, the relatively low R^2 in Fig. 6(b) indicates a large variance of predictive performance in certain regions. Specifically, for powder thicknesses $\delta < 180$ μm, the power law model shows a large variance as certain points are over-estimated by as much as over 200%. In application, this large error will cause the prediction algorithm to miss defects at low powder thickness levels since the algorithm tends to over-estimate powder thickness levels.

The consolidation of the five thermal history fitted parameters (A_1, A_2, β_1, β_2, and t_i) fitted thermal history to the rise time can lead to some loss of information. Generating physics based correlations with all five parameters is challenging. Machine learning techniques are well suited to this type of problem, provided sufficient data is available. A feed-forward neural network (FNN) is applied to the data in Fig. 5 using the Regression Learner toolbox in MATLAB. The five parameters A_1, A_2, β_1, β_2, and t_i in Fig. 5(e)-(i) are directly used to train the FNN to predict the powder layer thickness.

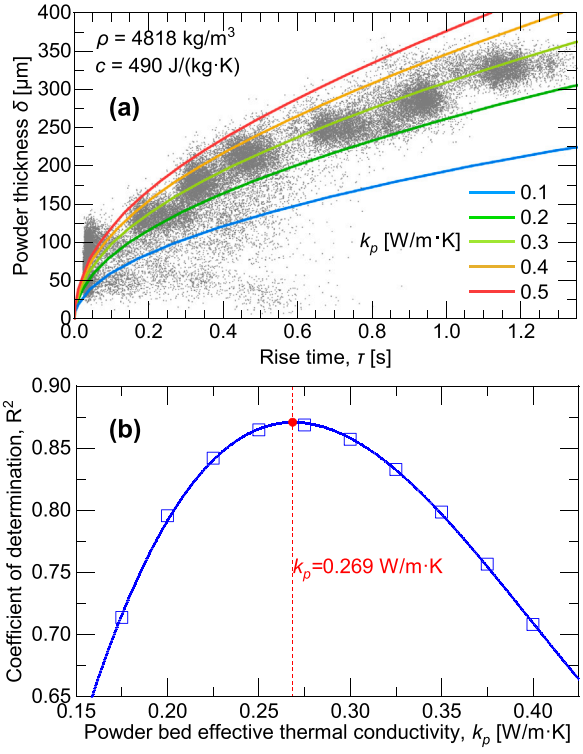

Fig. 7. (a) Effect of powder layer effective thermal conductivity on simulated rise time/powder layer thickness relationship (b) dependence of coefficient of determination R^2 for power law fitted rise time/powder layer thickness relationship with respect to powder layer effective thermal conductivity.

The general structure of an FNN model can be mathematically represented by the following equations

$$\begin{aligned} \textit{input layer}: a_j^{[1]} &= \sigma^{[1]}\left(\sum_{i=1}^{n^{[1]}} w_{ij}^{[1]} x_i + b^{[1]}\right) \\ \textit{hidden layer}: a_j^{[l-1]} &= \sigma^{[l-1]}\left(\sum_{i=1}^{n^{[l-1]}} w_{ij}^{[l-1]} a_j^{[l-2]} + b^{[l-1]}\right) \\ \textit{output layer}: y_j &= \sigma^{[l]}\left(\sum_{i=1}^{n^{[l]}} w_{ij}^{[l]} a_j^{[l-1]} + b^{[l]}\right) \end{aligned} \tag{12}$$

where x_i is input features and y_j is the desired output target. $w_{ij}^{[k]}$ is the weight from neuron i of the k-1 layer to neuron j of the k layer. l and $n^{[k]}$ denote the number of layers and number of neurons for the k layer, respectively. $b^{[k]}$ and $\sigma^{[k]}$ are the bias and activation function for the k layer.

In this study, there are 42,510 total data points that are split based on a ratio of 70–15–15 into the training, validation, and testing dataset for the FNN, respectively. The training dataset is used to adjust the weights and biases of the FNN, the validation dataset is used to adjust the hyperparameters (number neurons) of the FNN, and the testing dataset is used to evaluate the performance of the FNN to an unseen dataset. It is important to note that data splitting is conducted before any further data processing steps such as normalization and scaling to prevent data leakage. Using the regression learner MATLAB toolbox, several different FNN architectures are tested against each other with their own specifications. A model with a single hidden layer with 100 hidden neurons and ReLu as the activation function displayed the best performance with an R-squared value of 0.962.

Fig. 8 compares the prediction results from the rise time only correlation and the five parameters based FNN. The FNN preforms significantly better for thinner powder layers. The overall coefficient of determination R^2 improves to 0.962 for the FNN as opposed to 0.859 using the rise time correlation. Fig. 8(c) shows histograms of the true powder thicknesses when the predicted powder layer thickness is $\delta_p = 200 \pm 5$ μm. Fitting a normal distribution to the results from both models gives a 95% confidence interval estimate of the true powder layer thickness of $\delta = 194.2 \pm 60.6$ μm for the rise time correlation which is improved to $\delta = 201.5 \pm 32.2$ μm for the FNN model.

6. In-situ thermographic monitoring for recoater interaction

Thermal distortion occurs commonly in LPBF. This can occur for unsupported parts when there is inadequate conduction to the build plate leading to excessive heating. The distortion lowers the powder thickness on next layer which exasperates the overheating as less material is melted. When the distortion of the part causes it to break through the powder layer, it can interact with the recoater. The interaction of the recoater with the part can abrade a soft wiper while a rigid wiper can crash into the part and damage the machine, part, or both. In the case of a flexible wiper, the abraded area allows an increase in the powder layer thickness for every part in-line with the abraded area. The contact with the wiper is potentially catastrophic for both types of wipers. Detecting thermal distortion prior to a part breaking through the powder layer allows the local process parameters to be adjusted in order to limit distortion or to have the part suppressed to save the build. The distorted part leads to a change in the local powder layer thickness which can be detected using the thermographic powder layer monitoring technique.

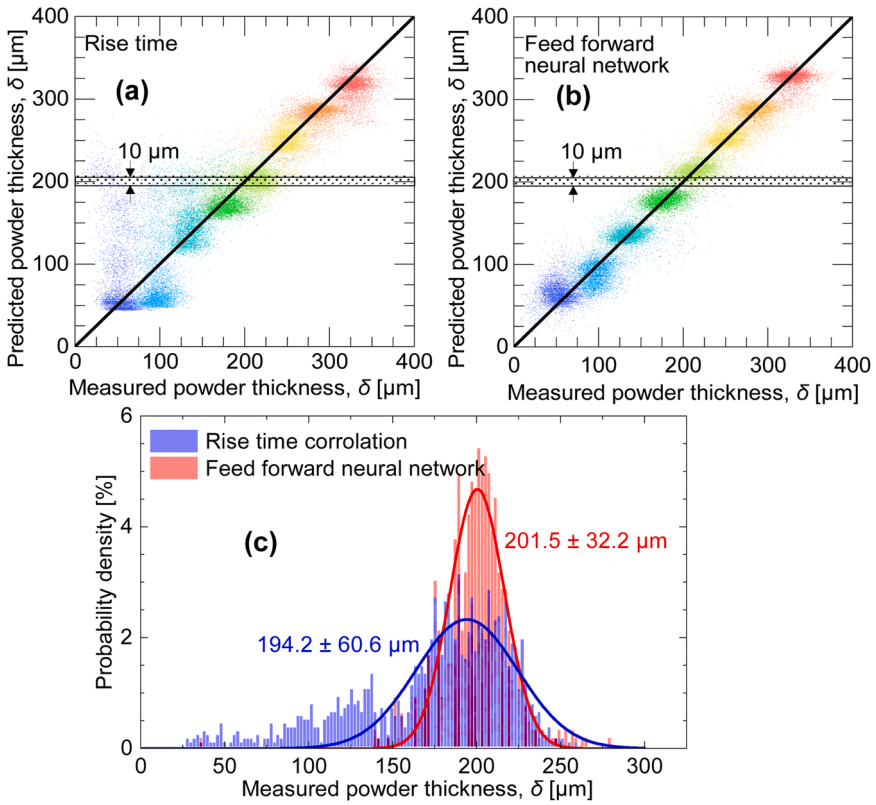

Fig. 8. Predicted powder thickness δ by using (a) rise time method, (b) neural network regression method and (c) powder thickness with normal distribution when the predicted powder layer thickness is $\delta_p = 200 \pm 5$ μm.

Artifacts with an overhang are printed to demonstrate a change in powder layer thickness caused by thermal stress as reported in our previous work [42]. The dimensions of the overhang artifact are shown in Fig. 9(a). Fig. 9(b) shows a photograph of the specimen and a block printed with the Renishaw AM250 system using a flexible (silicone) wiper. The block is added behind the specimen to capture any subsequent changes in the powder bed thickness due to the abraded wiper. These artifacts are printed using nominal process parameters developed for stainless steel 304 L. Specifically, a laser power of 200 W, beam size of 75 μm, scan speed of 800 mm/s and setup nominal powder thickness $\delta_N = 50$ μm. For simplicity, the laser was only rastered in the x-direction. The parts in Fig. 9(b) were stopped after 219 layers and show significant distortion in the unsupported overhanging region.

The height of the powder layer is monitored using the thermal camera, the temperature history for each point fitted using the 5-parameters in Fig. 5, and the FNN used to predict the powder layer thickness. Fig. 10(a) shows the predicted powder thickness averaged along the leading edge of the overhang artifact (red line). For reference, the predicted powder thickness averaged over a line at the center of each layer (blue line) is also plotted. The constant raster direction leads to a slightly higher part (lower thickness) at the edge almost immediately. This is stable by layer 40. The powder layer thickness on the unsupported edge starts decreasing more and more at layer 180 due to thermal distortion. Over the entire print, the reference thickness in the center of the part is stable.

To verify these predictions, specimens were stopped at intermediate heights during the build. Photographs of the specimens stopped at layers 50, 140, and 215 are shown in Fig. 10(a). At the conclusion of the build, these parts were laser scanned (after removing powder but without removing the parts from the build plate). The nominal height is calculated by multiplying the number of layers with the nominal powder layer thickness. The actual powder layer thickness is this nominal height minus the laser scanner measured height. This thickness is plotted for both the unsupported edge and center of the part in Fig. 10(a) as points, by averaging the data measured over each line (red dash line or blue dash line) for the various layers. This validation was repeated for three different parts (stopped at the same layer) and the error bars show the standard deviations. The figure shows that the predicted layer height from the thermal inspection method agrees well with the measured height. In particular, the thermal distortion predicted that the part broke

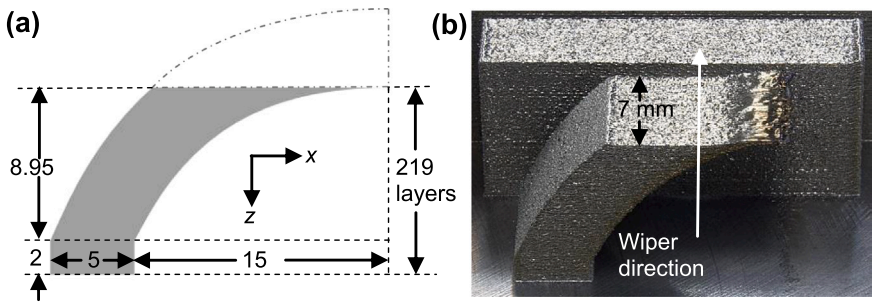

Fig. 9. (a) Schematic image of overhang with dimensions in mm (b) photograph of distortion grows on the overhang top surface with a block behind it.

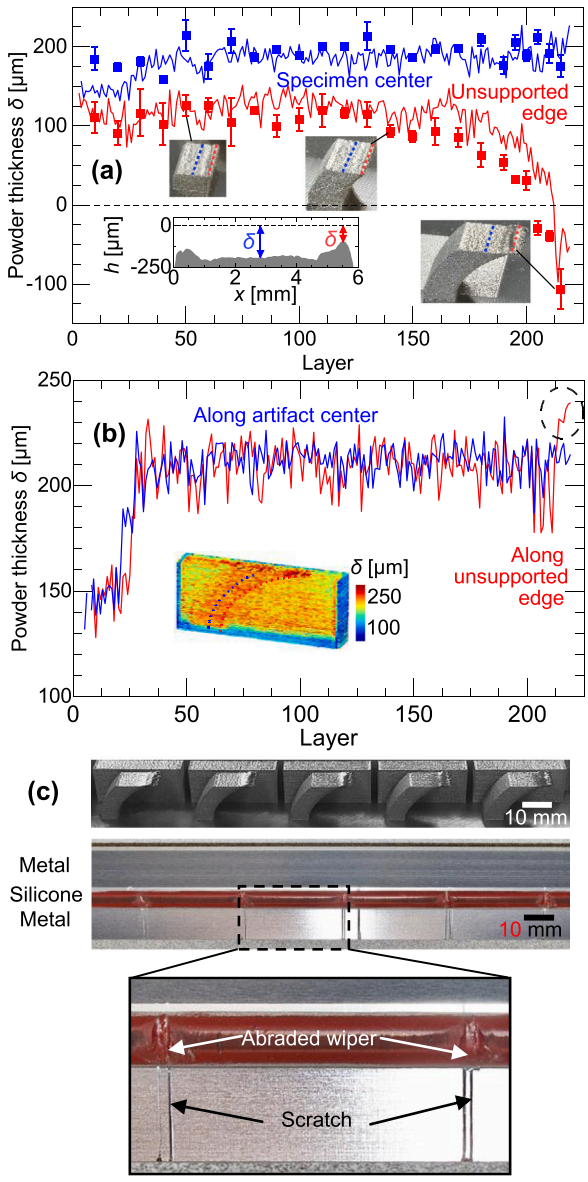

Fig. 10. (a) Comparison of powder thickness δ between thermal measure and height measure. The blue line indicates the inner center powder thickness averaged over the blue dots line for every layer. The red line denotes the unsupported edge powder thickness averaged over the red dots line for every layer. (b) Powder thickness δ at different block areas. Blue and red lines represent the powder thickness of block along blue and red dots with respect to layers. The insert images are the 3D map of block powder thickness δ obtained from the thermal measure. (c) Final overhang samples and the abraded wiper.

through the powder layer at layer 212 while the measurements show a broke-through between layers 200 and 205.

Fig. 10(b) shows the thermal inspection predicted height for the block behind the overhang artifact. The predicted powder layer height is plotted for the same x-position as the traces in Fig. 10(a) (immediately behind the leading edge of the artifact and at its center). The powder layer stabilizes by layer 40. At layer 215, the local powder layer thickness behind the unsupported edge starts to increase dramatically. This is due to the abrasion of the wiper and leads to the local deposition of more powder. While not visible in the photograph of the part in Fig. 9(b), if this continued, it could negatively affect the local part properties.

Fig. 10(c) shows photographs of five identical parts, stopped at layer 219, and the wiper. The damage to the wiper is visible (scratched metal and abraded silicone). The decrease in the powder layer thickness indicating an imminent crash could be detected by layer 190 from the thermal inspection estimate. This is at least 10 layers before the collision and would allow the part to be suppressed to prevent damage to the wiper as well as any other parts in the build.

It is interesting to observe that the measured as well as predicted powder layer thicknesses are so much larger than the nominal powder layer thickness, about 200 and 50 μm, respectively. This is consistent with Mahmoodkhani et al. [11] who showed a nominal powder thickness of 20 μm resulted in a measured powder layer thickness of more than 100 μm as well as Wischeropp et al. [12] who showed nominal powder layer thicknesses of 30 and 50 μm corresponded to actual thicknesses of 165 and 225 μm. This phenomenon is the result of shrinkage of powder consolidation over multiple layers [11] in addition to significant losses of the powder from spatter and denudation [12].

In addition to suppressing a bad part before it breaks through, detecting thermal distortion early could be used to adjust the process parameters to match the reduced powder layer thickness. This includes lowering the laser power or increasing the scan speed. There is also the possibility to adjust the scan path to minimize overheating. Because the distortion is detected early, there is time to react by making more gradual changes. Other more drastic approaches are possible, including laser ablation of the distorted region or physically deforming it down.

7. Conclusion

This paper demonstrates the potential of using in-situ thermographic inspection to evaluate the powder layer thickness and estimate local powder layer thermal properties. An experimental study, conducted using realistic process parameters in a commercial LPBF machine, agrees well with a 1D thermal diffusion model for the powder layer. This uses a stationary LWIR thermal camera in a staring configuration. A parametric fit of the temperature history is used to generate a correlation to the powder layer thickness. A simplified rise time model provides insight and was used to estimate thermal conductivity, but it was outperformed by a FNN machine learning method for data obtained from a calibration specimen. This was tested for a simple artifact with an overhanging unsupported edge. Without underlying supported structure, the ability of the overhang to dissipate heat is significantly reduced, causing heat to build up at the edge. Overheating causes thermal distortion, which reduces the thickness of the next powder layer. The overheating is exasperated as there is less powder for the laser to melt and the distortion rapidly increases to the point where it breaks through the powder layer and produces the abrasion of the silicone wiper. The FNN model was applied to monitor thermal distortion and could ultimately predict a wiper collision at least 10 layers before it occurred.

The thermal inspection method appears to have several advantages relative to existing methods for monitoring the powder layer in-situ. In particular, because the inspection occurs during the recoating step, it does not add additional processing time for the inspection. Comparing with optical coherence tomography and fringe projection methods, this method's additional equipment costs are minimal. The thermographic inspection technique was able to resolve the powder layer height to $\pm$ 32.2 μm (within the mean particle diameter).

Future work will include the development of automatic part suppression algorithms as well as providing feedback to try to minimize thermal distortion. In addition, the ability to certify additional aspects of the powder bed health will also be expanded. For example, variances in the powder size distribution can be detected by identifying changes in the local thermal properties of the bed. While quantitative measurements require training, the thermographic inspection technique can reveal local deviations from the standard thermal history in the bed. This approach extends to other aspects of the LBPF process including the gas flow over the powder bed. This study also suggests that other techniques from thermographic based non-destructive testing, including active thermography, may add significant insight to the LBPF process.

Disclaimer

This report was prepared as an account of work sponsored by an agency of the United States Government. Neither the United States government nor any agency thereof, nor any of its employees, makes any warranty, express or implied, or assumes any legal liability or responsibility for the accuracy, completeness or usefulness.

CRediT authorship contribution statement

Tao Liu: Conceptualization, Methodology, Investigation, Software, Data curation, Validation, Writing – original draft. **Cody S. Lough:** Investigation. **Hossein Sehhat:** Investigation. **Yi Ming Ren:** Software, Data curation, Writing – original draft. **Panagiotis D. Christofides:** Supervision. **Edward C. Kinzel:** Conceptualization, Methodology, Supervision, Writing – Original Draft, Writing – Review & Editing. **Ming C. Leu:** Conceptualization, Methodology, Supervision, Writing – Review & Editing.

Declaration of Competing Interest

The authors declare that they have no known competing financial interests or personal relationships that could have appeared to influence the work reported in this paper.

Acknowledgments

This material is based upon work supported by the U.S. Department of Energy's Office of Energy Efficiency and Renewable Energy (EERE) under the Advanced Manufacturing Office Award Number DE-EE0007613. The financial support is through the Clean Energy Smart Manufacturing Innovation Institute (CESMII), with Honeywell being the primary recipient of this award. The authors are also grateful to the Kansas City National Security Campus for furnishing the Renishaw AM250 system used in this research.

Appendix A. Supporting information

Supplementary data associated with this article can be found in the online version at doi:10.1016/j.addma.2022.102873.

References

[1] Q.B. Nguyen, D.N. Luu, S.M.L. Nai, Z. Zhu, Z. Chen, J. Wei, The role of powder layer thickness on the quality of SLM printed parts, Arch. Civ. Mech. Eng. 18 (2018) 948–955.
[2] H. Chen, Q. Wei, Y. Zhang, F. Chen, Y. Shi, W. Yan, Powder-spreading mechanisms in powder-bed-based additive manufacturing: Experiments and computational modeling, Acta Mater. 179 (2019) 158–171.
[3] Q. Han, H. Gu, R. Setchi, Discrete element simulation of powder layer thickness in laser additive manufacturing, Powder Technol. 352 (2019) 91–102.
[4] M.H. Sehhat, A. Mahdianikhotbesara, Powder spreading in laser-powder bed fusion process, Granul. Matter 23 (2021) 89.
[5] Z. Zhang, U. Ali, Y. Mahmoodkhani, Y. Huang, S.I. Shahabad, A.R. Kasinathan, E. Toyserkani, Experimental and numerical investigation on the effect of layer thickness during laser powder-bed fusion of stainless steel 17-4PH, Int. J. Rapid. Manuf. 9 (2020) 212–230.
[6] M. Ma, Z. Wang, M. Gao, X. Zeng, Layer thickness dependence of performance in high-power selective laser melting of 1Cr18Ni9Ti stainless steel, J. Mater. Process. Tech. 215 (2015) 142–150.
[7] K. Kempen, E. Yasa, L. Thijs, J.-P. Kruth, J.V. Humbeeck, Microstructure and mechanical properties of Selective Laser Melted 18Ni-300 steel, Phys. Proc. 12 (2011) 255–263.
[8] C. Qiu, C. Panwisawas, M. Ward, H.C. Basoalto, J.W. Brooks, M.M. Attallah, On the role of melt flow into the surface structure and porosity development during selective laser melting, Acta Mater. 96 (2015) 72–79.
[9] V.Sh Sufiiarov, A.A. Popovich, E.V. Borisov, I.A. Polozov, D.V. Masaylo, A.V. Orlov, The effect of layer thickness at selective laser melting, Procedia Eng. 174 (2017) 126–134.
[10] J.S. Weaver, J. Whiting, V. Tondare, C. Beauchamp, M. Peltz, J. Tarr, T.Q. Phan, M. A. Donmez, The effects of particle size distribution on the rheological properties of the powder and the mechanical properties of additively manufactured 17-4 PH stainless steel, Addit. Manuf. 39 (2021), 101851.
[11] Y. Mahmoodkhani, U. Ali, S.I. Shahabad, A.R. Kasinathan, R. Esmaeilizadeh, A. Keshavarzkermani, E. Marzbanrad, E. Toyserkani, On the measurement of effective powder layer thickness in laser powder-bed fusion additive manufacturing of metals, Prog. Addit. Manuf. 4 (2019) 109–116.
[12] T.M. Wischeropp, C. Emmelmann, M. Brandt, A. Pateras, Measurement of Actual Powder Layer Height and Packing Density in a Single Layer in Selective Laser Melting, Addit. Manuf. 28 (2019) 176–183.
[13] B. Vrancken, Study of Residual Stresses in Selective Laser Melting, 2016.
[14] M.F. Zaeh, G. Branner, Investigations on residual stresses and deformations in selective laser melting, Prod. Eng. 4 (2010) 35–45.
[15] J.P. Kruth, J. Deckers, E. Yasa, R. Wauthlé, Assessing and comparing influencing factors of residual stresses in selective laser melting using a novel analysis method, Proc. Inst. Mech. Eng. Part. B. J. Eng. Manuf. 226 (2012) 980–991.
[16] H.A. Kumar, S. Kumaraguru, Distortion in Metal Additive Manufactured Parts, 3D Printing and Addit. Manuf. Technol, Springer,, Singapore, 2019, pp. 281–295.
[17] M. Abdelrahman, E.W. Reutzel, A.R. Nassar, T.L. Starr, Flaw detection in powder bed fusion using optical imaging, Addit. Manuf. 15 (2017) 1–11.
[18] F. Caltanissetta, M. Grasso, S. Petrò, B.M. Colosimo, Characterization of in-situ measurements based on layerwise imaging in laser powder bed fusion, Addit. Manuf. 24 (2018) 183–199.
[19] R.J. Williams, C.M. Davies, P.A. Hooper, In situ monitoring of the layer height in laser powder bed fusion, Mater. Des. Process Commun. (2020) 1–5.
[20] P.J. DePond, G. Guss, S. Ly, N.P. Calta, D. Deane, S. Khairallah, M.J. Matthews, In situ measurements of layer roughness during laser powder bed fusion additive manufacturing using low coherence scanning interferometry, Mater. Des. 154 (2018) 347–359.
[21] Z. Li, X. Liu, S. Wen, P. He, K. Zhong, Q. Wei, Y. Shi, S. Liu, In Situ 3D Monitoring of Geometric Signatures in the Powder-Bed-Fusion Additive Manufacturing Process via Vision Sensing Methods, Sensors 18 (2018) 1180.
[22] B. Zhang, J. Ziegert, F. Farahi, A. Davies, In situ surface topography of laser powder bed fusion using fringe projection, Addit. Manuf. 12 (2016) 100–107.
[23] N.M. O'Dowd, A.J. Wachtor, M.D. Todd, Effects of digital fringe projection operational parameters on detecting powder bed defects in additive manufacturing, Addit. Manuf. 48 (2021), 102454.
[24] S.D. Holland, R.S. Reusser, Material Evaluation by Infrared Thermography, Annu. Rev. Mater. Res. 46 (2015) 1–17.
[25] A. Salazar, A. Mendioroz, E. Apiñaniz, C. Pradere, F. Noël, J.C. Batsale, Extending the flash method to measure the thermal diffusivity of semitransparent solids, Meas. Sci. Technol. 25 (3) (2014), 035604.
[26] R. Shrestha, W. Kim, Evaluation of coating thickness by thermal wave imaging: A comparative study of pulsed and lock-in infrared thermography – Part I: Simulation, Infrared Phys. Tech. 83 (2017) 124–131.
[27] F. Maier, B.G. Zagar, Measurement of paint coating thickness by thermal transient method, IEEE T. Instrum. Meas. 58 (2009) 1958–1966.
[28] T. Rashid, H.A. Khawaja, K. Edvardsen, Measuring thickness of marine ice using IR thermography, Cold Reg. Sci. Technol. 158 (2019) 221–229.
[29] R.A. Osornio-Rios, J.A. Antonino-Daviu, R. de J. Romero-Troncoso, Recent industrial applications of infrared thermography: a review, IEEE T. Ind. Inf. 15 (2018) 615–625.
[30] F. Ciampa, P. Mahmoodi, F. Pinto, M. Meo, Recent advances in active infrared thermography for non-destructive testing of aerospace components, Sensors 18 (2018) 609.
[31] H. Halloua, A. Elhassnaoui, A. Saifi, A. Elamiri, A. Obbadi, Y. Errami, S. Sahnoun, Neural networks and genetic algorithms for the evaluation of coatings thicknesses in thermal barriers by infrared thermography data, Procedia Struct. Integr. 5 (2017) 997–1004.
[32] S. Ranjit, Y. Chung, W. Kim, Thermal behavior variations in coating thickness using pulse phase thermography, J. Korean Soc. Nondestruct. Test. 36 (2016) 259–265.
[33] B. Lane, E. Whitenton, S. Moylan, Multiple sensor detection of process phenomena in laser powder bed fusion, Proc. SPIE 9861 (2016), 986104.
[34] J.C. Heigel, E. Whitenton, Measurement of thermal processing variability in powder bed fusion, 2018 ASPE Euspen Summer Top. Meet. - Adv. Precis. Addit. Manuf. (2018) 242–247.
[35] P.A. Hooper, Melt pool temperature and cooling rates in laser powder bed fusion, Addit. Manuf. 22 (2018) 548–559.
[36] B.M. Colosimo, E. Grossi, F. Caltanissetta, M. Grasso, Penelope: A Novel Prototype for In Situ Defect Removal in LPBF, Jom-Us 72 (2020) 1332–1339.
[37] M. Grasso, B.M. Colosimo, A statistical learning method for image-based monitoring of the plume signature in laser powder bed fusion, Robot. Cim. -Int. Manuf. 57 (2019) 103–115.
[38] R. Yavari, R. Williams, A. Riensche, P.A. Hooper, K.D. Cole, L. Jacquemetton, H. (Scott), Halliday, P.K. Rao, Thermal modeling in metal additive manufacturing using graph theory – Application to laser powder bed fusion of a large volume impeller, Addit. Manuf. 41 (2021), 101956.
[39] M.R. Yavari, R.J. Williams, K.D. Cole, P.A. Hooper, P. Rao, Thermal Modeling in Metal Additive Manufacturing Using Graph Theory: Experimental Validation With Laser Powder Bed Fusion Using In Situ Infrared Thermography Data, J. Manuf. Sci. Eng. 142 (2020), 121005.
[40] Y.M. Ren, Y. Ding, Y. Zhang, P.D. Christofides, A three-level hierachical framework for additive manufacturing, Digit. Chem. Eng. 1 (2021), 100001.
[41] H. Elwarfalli, D. Papazoglou, D. Erdahl, A. Doll, J. Speltz, In Situ Process Monitoring for Laser-Powder Bed Fusion using Convolutional Neural Networks and Infrared Tomography, IEEE Natl. Aerosp. Electron. Conf. (2019) 323–327.
[42] Y.M. Ren, Y. Zhang, Y. Ding, T. Liu, C.S. Lough, M.C. Leu, E.C. Kinzel, P. D. Christofides, Finite element modeling of direct metal laser solidification process:

Sensor data replication and use in defect detection and data reduction via machine learning, Chem. Eng. Res. Des. 171 (2021) 254–267.
[43] Z. Li, Z. Zhang, J. Shi, D. Wu, Prediction of surface roughness in extrusion-based additive manufacturing with machine learning, Robot Cim. -Int Manuf. 57 (2019) 488–495.
[44] E.I. Alrashydah, S.A. Abo-Qudais, Modeling of creep compliance behavior in asphalt mixes using multiple regression and artificial neural networks, Constr. Build. Mater. 159 (2018) 635–641.
[45] M.R. Alkahari, T. Furumoto, T. Ueda, A. Hosokawa, R. Tanaka, M.S.A. Aziz, Thermal conductivity of metal powder and consolidated material fabricated via selective laser melting, Key Eng. Mater. 523–524 (2012) 244–249.
[46] L.C. Wei, L.E. Ehrlich, M.J. Powell-Palm, C. Montgomery, J. Beuth, J.A. Malen, Thermal conductivity of metal powders for powder bed additive manufacturing, Addit. Manuf. 21 (2018) 201–208.